Check for updates

ADVANCED MATERIALS
www.advmat.de

High-Entropy Co-Free O3-Type Layered Oxyfluoride: A Promising Air-Stable Cathode for Sodium-Ion Batteries

*Akanksha Joshi, Sankalpita Chakrabarty, Sri Harsha Akella, Arka Saha, Ayan Mukherjee, Bruria Schmerling, Michal Ejgenberg, Rosy Sharma, and Malachi Noked**

Sodium-ion batteries have recently emerged as a promising alternative to lithium-based batteries, driven by an ever-growing demand for electricity storage systems. The present workproposes a cobalt-free high-capacity cathode for sodium-ion batteries, synthesized using a high-entropy approach. The high-entropy approach entails mixing more than five elements in a single phase; hence, obtaining the desired properties is a challenge since this involves the interplay between different elements. Here, instead of oxide, oxyfluoride is chosen to suppress oxygen loss during long-term cycling. Supplement to this, lithium is introduced in the composition to obtain high configurational entropy and sodium vacant sites, thus stabilizing the crystal structure, accelerating the kinetics of intercalation/deintercalation, and improving the air stability of the material. With the optimization of the cathode composition, a reversible capacity of 109 mAh g^{-1} (2–4 V) and 144 mAh g^{-1} (2–4.3 V) is observed in the first few cycles, along with a significant improvement in stability during prolonged cycling. Furthermore, in situ and ex situ diffraction studies during charging/discharging reveal that the high-entropy strategy successfully suppresses the complex phase transition. The impressive outcomes of the present work strongly motivate the pursuit of the high-entropy approach to develop efficient cathodes for sodium-ion batteries.

1. Introduction

Lithium-ion batteries (LIBs) have already become ubiquitous in modern societies as they have permeated our daily life through portable electronic devices and electric vehicles.[1] However, the scarcity of lithium resources and their concentration in geopolitically sensitive areas have pushed researchers to explore other options. In this surge to find an alternative chemistry for electrochemical energy storage, sodium-ion batteries have come into the limelight on account of the huge abundance of sodium resources and the operational similarities between sodium-ion batteries and LIBs.[2,3] Replacing lithium with sodium may seem easy given their similar chemical characteristics, but random disclosures are often found due to the unknown interaction of host structure depending on sodium and lithium intercalation/de-intercalation as sodium ion exhibits large ionic size as compared to lithium ion.[4]

Various cathode materials for sodium-ion batteries have been explored, including oxides,[5–7] Prussian blue analogs,[8] and polyanionic compounds.[9,10] Among them, layered oxides (Na_xMO_2, where M is a 3d metal, categorized as O-type or P-type, typically a P2 or O3 phase) have emerged as promising materials, mainly because of their ability to facilitate rapid and reversible sodium-ion intercalation/deintercalation during charge/discharge through their structurally embedded 2D channels.[11] However, layered oxide materials are associated with complex phase transitions, structural instability, and severe oxygen redox activity at high voltage, which restricts their overall applicability. Compared to the P2 phase, the O3 phase of layered oxides can accommodate a larger number of Na^+ ions in the structure, which results in higher capacity.[12] However, the O3 phase has its own drawbacks: its complex phase transition during charging/discharging results in structural deterioration, declining capacity retention, low rate capability, and poor air stability.[13] Furthermore, considerable attention has been focused on reducing the use of cobalt in electrode materials, in view of resource limitations and geopolitical issues.[14]

All the aforementioned challenges could be mitigated by rationally tailoring the material structure. A relatively new yet promising concept, the "high-entropy approach" is one such strategy

A. Joshi, S. Chakrabarty, S. H. Akella, A. Saha, B. Schmerling, M. Ejgenberg, M. Noked
Department of Chemistry
Institute of Nanotechnology and Advanced Materials (BINA)
Bar-Ilan University
Ramat Gan 5290002, Israel
E-mail: Malachi.Noked@biu.ac.il
A. Mukherjee
Department of Hydro and Electro Metallurgy
CSIR-Institute of Minerals and Materials Technology Bhubaneswar
Bhubaneswar, Odisha 751013, India
R. Sharma
Department of Chemistry
Indian Institute of Technology (Banaras Hindu University)
Varanasi 221005, India

The ORCID identification number(s) for the author(s) of this article can be found under https://doi.org/10.1002/adma.202304440

© 2023 The Authors. Advanced Materials published by Wiley-VCH GmbH. This is an open access article under the terms of the Creative Commons Attribution License, which permits use, distribution and reproduction in any medium, provided the original work is properly cited.

DOI: 10.1002/adma.202304440

that can help stabilize the performance of O3-type cathodes by maximizing the configuration entropy of the structure. The high-entropy approach relies on the "mixing" of more than five metals that share the same crystallographic site in a single-phase crystal structure.[15] Higher entropy increases the solid solubility of the different metals in the structure, which in turn supports the formation of a single phase.[16] Various high-entropy materials intended for various applications have been reported over the past few years,[17,18] mostly high-entropy oxides (HEOs).[19–21]

The "High Entropy (HE)" effect is helpful in tackling the above-mentioned issues of the O3-layer structure in various ways. Yeh et al.[22] have listed four factors that affect the properties of high-entropy materials, namely, configuration entropy, lattice distortion, sluggish diffusion, and the cocktail effect. Configurational entropy beyond $1.5R$ (where R is the ideal gas constant) is the deciding criterion for the formation of a high-entropy crystal structure; it is derived from the Boltzmann and Gibbs interpretation of entropy.[23,24] From the Gibbs–Helmholtz equation, an increase in entropy leads to a reduction in Gibbs free energy (ΔG), which is associated with an improvement in structural stability.[25] However, amongst "cocktail effect" via integration of a number of elements embraces the stronger impact on the properties as every element has a distinctive impact on the properties of the structure. By selecting the elements in its structure and adjusting their concentrations, a high-entropy material can be tailored according to the desired properties. Some studies have also concluded that the HE strategy enhances the diffusion of Na^+ ions by suppressing short-range order in the structure.[26,27] Berardan et al.[28] have also demonstrated superionic conductivity in some HE oxides (for Li^+: $>10^{-3}$ S cm^{-1}; for Na^+: $\approx 5 \times 10^{-6}$ S cm^{-1}); another motivating factor for further research in HE materials for battery application. Furthermore, the obvious lattice distortion due to different ionic sizes in the structure also impacts its mechanical properties.

Employing the HE strategy to design a cathode is a complex task as it involves the interplay between the contributions of every element to its capacity and degradation during cycling must be avoided. Here, we aimed to strike a balance between the capacity and structural stability of the material by incorporating both redox-active and non-active transition metals (TMs) in its structure. All the TMs were rationally selected, keeping in view factors such as similarity in ionic size, chemical compatibility, and redox compatibility.[26] Because the chemical compatibility of Mg^{2+} with other TMs is poor,[26] its concentration was kept low in the designed cathode.

The combination of six TMs dilutes the concentration of each TM; in order to maintain enough redox activity, the concentration of redox-active metal species (here: Ni^{2+}, Fe^{3+}, and Mn^{2+}) must be sufficiently large, at the expense of non-active TM species. Li^+ was added to the composition with the intention of stabilizing the structure and improving Na^+ diffusion because Li^+ has been shown to promote the superlattice structure by reversible hopping between the Na^+ layer and TM layer during charging/discharging.[29,30] Besides, Li^+ has a smaller ionic radius than Na^+ and similar properties, facilitating the substitution of Li^+ for Na^+, with an associated reduction in the total molecular weight of the composition.[31] The introduction of Li^+ creates vacant Na^+ sites in the structure, which further helps reduce the barrier for Na^+ diffusion.

In addition, we selected oxyfluorides over oxides for their ability to suppress oxygen loss during long-term cycling; because the M—F bond has a more ionic nature than the M—O bond, the working potential is also expected to be increased.[26,32]

The general issue of poor air stability of layered materials is also addressed in this work; a large interlayer space and low Na content allow the insertion of water and carbonate ions into the TMO_2 slabs, which is the main reason for poor air stability.[33,34] Therefore, we chose an O3 structure, to which we added Mg to decrease the interlayer distance.[35] We added Li to increase the valence state of the TMs[36] and thus increase the oxidation resistance of the material and obtain an air-stable structure.

The designed high-entropy (HE) cathode exhibits a high reversible initial discharge capacity and a remarkably stable cycle life. Structural changes were studied through ex situ and in situ XRD studies, and charge compensation was studied through an ex situ XPS study. Ex situ and in situ, XRD studies also demonstrate reversible structural changes at the end of the discharge cycle and after extended cycling. As it is well known that P-type structures clearly possess better rate capability and structural integrity than O-type,[37,38] and for this cathode, most of the capacity is in the P-type region. Hence, the P3–O3 transition is effectively suppressed, which promotes a high-rate performance. Furthermore, an online electrochemical mass spectrometry study (OEMS) was also carried out on the High entropy (HE) cathode; showing negligible oxygen loss even at high potential. In the present work, we focused on increasing the capacity of a cobalt-free cathode while maintaining good air stability. The HE concept is still in its nascent phase, with the challenges that this entails; this work is an attempt to explore the potential of this concept by rationally selecting metals to design a cathode with targeted properties for its application in sodium-ion batteries.

2. Results and Discussion

In the present work, a high-entropy-based cathode material was designed and synthesized by combining six TM cations (Ni^{2+}, Fe^{3+}, Mn^{2+}, Ti^{4+}, Mn^{4+}, and Mg^{2+}) and two alkali-metal cations (Li^+ and Na^+) in different stoichiometries; O and F were used as the counter anions. The cations were carefully chosen to incorporate two major benefits: i) Ni^{2+}, Fe^{3+}, and Mn^{2+} for charge compensation during sodium-ion intercalation/deintercalation and ii) Ti^{4+}, Mn^{4+}, and Mg^{2+} for structural stabilization. The high-entropy oxyfluoride (HEO-F) material with the general formula of $Na_xLi_yNi^{2+}_{0.4}Fe^{3+}_{0.2}Mn^{2+}_{0.4}Ti^{4+}_{0.04}Mn^{4+}_{0.04}Mg^{2+}_{0.02}O_{1.9}F_{0.1}$ (where, $x = 1$, 0.9, or 0.8 and $y = 0$, 0.1, or 0.2) was synthesized by solid-state reaction (Figure S1, Supporting Information). The proportions of TMs were rationally selected by considering critical factors such as ionic size, redox compatibility, and electroactivity.[26] Because Mg^{2+} is poorly compatible with other TMs, its concentration was kept low in the designed cathode. The incorporation of six TMs dilutes the concentration of each TM; therefore, to maintain sufficient redox activity, higher concentrations of the redox-active metal cations Ni^{2+}, Fe^{3+}, and Mn^{2+} were used compared to the non-active TMs.

Overall, this study aims to decipher how varying the amounts of Na and Li in the composition affects the structural, physical, and electrochemical characteristics of the HEO-F as a sodium-ion battery cathode material; a detailed analysis is presented in the

© 2023 The Authors. Advanced Materials published by Wiley-VCH GmbH

15214095, 2023, 51, Downloaded from https://onlinelibrary.wiley.com/doi/10.1002/adma.202304440 by Indian Institute Of Technology , Wiley Online Library on [16/04/2024]. See the Terms and Conditions (https://onlinelibrary.wiley.com/terms-and-conditions) on Wiley Online Library for rules of use; OA articles are governed by the applicable Creative Commons License

15214095, 2023, 51, Downloaded from https://onlinelibrary.wiley.com/doi/10.1002/adma.202304440 by Indian Institute Of Technology, Wiley Online Library on [16/04/2024]. See the Terms and Conditions (https://onlinelibrary.wiley.com/terms-and-conditions) on Wiley Online Library for rules of use; OA articles are governed by the applicable Creative Commons License

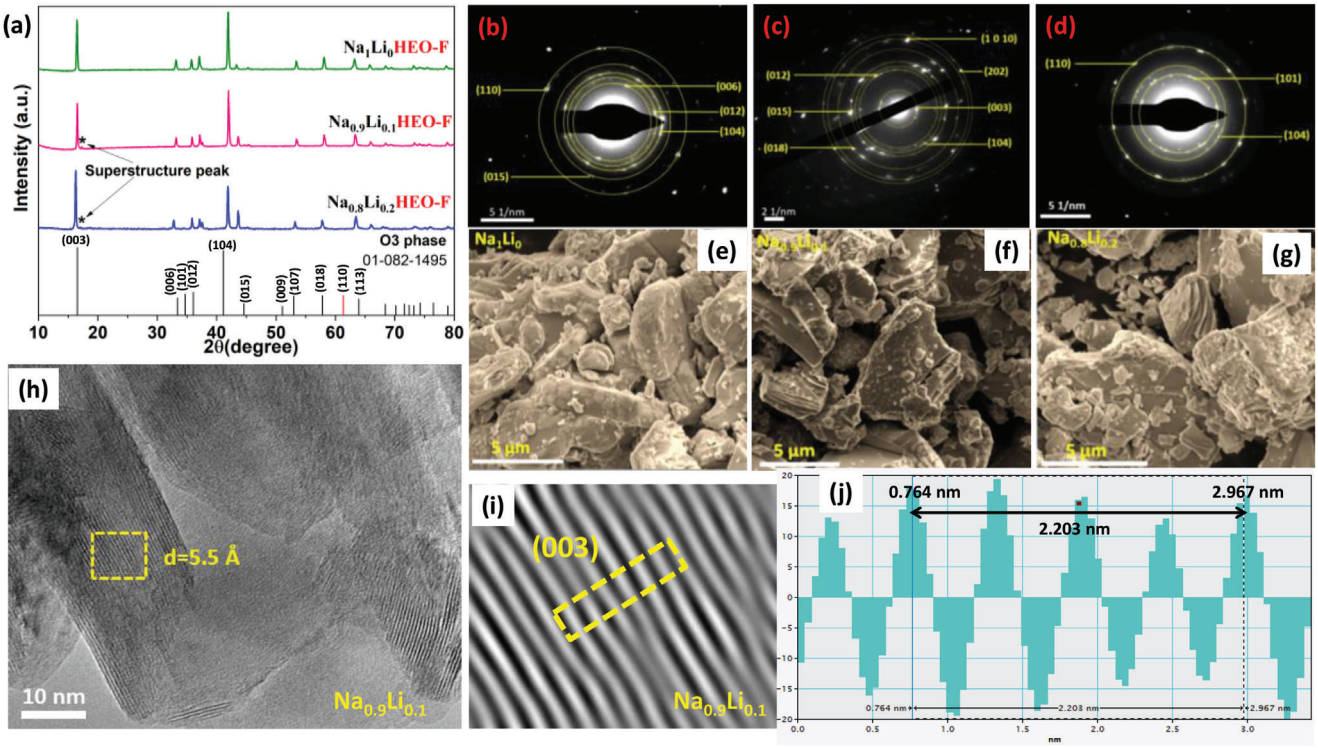

Figure 1. a) XRD pattern of the Na_xLi_y composition corresponding to the O3-phase layered structure. b–d) SAED patterns of Na_1Li_0 (b), $Na_{0.9}Li_{0.1}$ (c), and $Na_{0.8}Li_{0.2}$ (d). e–g) SEM images of Na_1Li_0 (e), $Na_{0.9}Li_{0.1}$ (f), and $Na_{0.8}Li_{0.2}$ (g). h) HRTEM image of $Na_{0.9}Li_{0.1}$ showing fringes of the (003) plane. i) Inverse FFT of the selected region of $Na_{0.9}Li_{0.1}$. j) Line profile of the selected line in the inverse FFT image.

following sections. Some compositions with different concentrations of Ni, Fe, and Mn were also studied to determine the role of these redox-active elements.

2.1. Crystal Structure and Morphology

To examine the composition of the synthesized HEO-F, ICP-OES analysis was carried out to confirm the compositions. The results tabulated in Table S2 (Supporting Information) confirm that Ni:Fe:Mn:Ti: Mg ratio is 0.4:0.2:0.44:0.04:0.02. Because the content of the other metals was identical in all samples, each sample was simply referred to as Na_xLi_y ($x = 1$, 0.9, or 0.8 and $y = 0$, 0.1, or 0.2), depending on its Na and Li content.

The entropy level of the material was then investigated by calculating another important parameter known as configurational entropy. For a material to be considered a high entropy material, its configurational entropy should be higher than $1.5R$.[23,24] The Na_1Li_0 composition has a configurational entropy value of $1.46R$, which falls in the category of medium entropy; with the addition of Li, it increases to $1.61R$ for $Na_{0.9}Li_{0.1}$ and $1.68R$ for $Na_{0.8}Li_{0.2}$ that confirms the formation of high-entropy structures.

The crystal structure of all three compositions was studied through XRD (**Figure 1**a), in which all the diffraction peaks are indexed to an O3-layered structure ($R\bar{3}m$ space group, JCPDS: 82-1495), with superstructure peaks ($LiTM_6$) at 17.2° and 43.6° in all Li compositions. The formation of a superstructure is ascribed to the mismatch in ionic valence and ionic radius of the various TMs, which results in ordering between Li and TM ions and a release of the developed strain in the structure.[38,39] Ionic size of Li is close to TM as compared to the large size Na^+ ion that results in Li occupancy at the transition metal site along with the alkali metal site. Chen and coworkers based on theoretical calculations reveal that Li at the TM site creates Na—O—Li configuration to boost the capacity consequent from anionic redox reaction whereas, Li at the alkali metal site forms LiO6 prismatic site to suppress the detrimental phase transformation.[40] The superstructure peak further indicates the occurrence of hopping of Li between Na and TM layers that leaves the empty sites at the Na layer and hence makes the Li-containing compositions Na deficient.

The (003) and (104) peaks were used to calculate the changes in lattice parameters and thus trace any structural changes. As shown in Figure S2 (Supporting Information), "*a*" decreases and "*c*" increases with increasing Li content in the structure. The contraction of the "*a*" parameter is associated with a decrease in the TM—O bond length and an increment in TM oxidation states, which was further confirmed by XPS[41–43] (Figures S3–S5, Supporting Information).; The average oxidation states in Na_1Li_0 are $Ni^{2.0+}$, $Mn^{2.0+}$, and $Fe^{2.11+}$. With the addition of Li, they increase to $Ni^{2.3+}$, $Mn^{2.6+}$, and $Fe^{2.16+}$ for $Na_{0.9}Li_{0.1}$ and $Ni^{2.32+}$, $Mn^{2.52+}$, and $Fe^{2.3+}$ for $Na_{0.8}Li_{0.2}$. The increase in "c" indicates the expansion of the adjacent layers. The results agree with those of Yuan and co-workers,[36] who reported that Na vacancies increase the valence state of the TM ions and hence

© 2023 The Authors. Advanced Materials published by Wiley-VCH GmbH

15214095, 2023, 51, Downloaded from https://onlinelibrary.wiley.com/doi/10.1002/adma.202304440 by Indian Institute Of Technology, Wiley Online Library on [16/04/2024]. See the Terms and Conditions (https://onlinelibrary.wiley.com/terms-and-conditions) on Wiley Online Library for rules of use; OA articles are governed by the applicable Creative Commons License

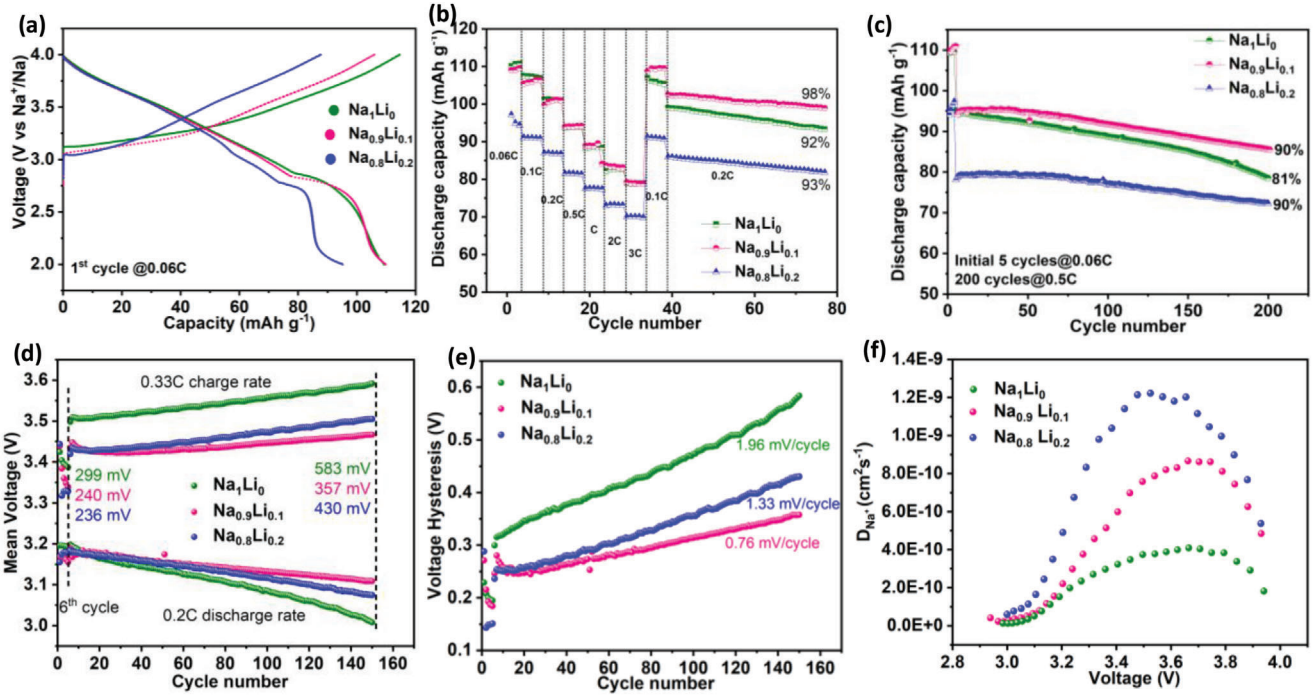

Figure 2. Comparative electrochemical performance in half-cells in the range 2–4 V vs Na/Na$^+$. a) First charge/discharge cycle at a rate of 0.06 C. b) Rate performance at different current rates. c) Long-term cycling performance at a discharge rate of 0.5 C after five pre-cycles at 0.06 C. d) Mean voltage profiles during charge (0.33 C) and discharge (0.5 C). e) Voltage hysteresis profiles are calculated from the difference between the mean charge and discharge voltages. f) Na^+ diffusion coefficient vs voltage profile, calculated from the GITT profile of the first formation cycle.

enhance the oxidation resistance of the material, which in turn suppresses unfavorable reactions between the material and the air.

Using the Rietveld refinement method on one of the compositions $Na_{0.9}Li_{0.1}$HEO-F, we determined the structure to be an O3-layered structure ($R\bar{3}m$ space group) in which all the TM ions are located at octahedral site (0 0 0.5) and Na occupies octahedral site (0 0 0) between the adjacent TM layers (Figure S6, Supporting Information). The ratio of the interlayer distance $d_{(O-Na-O)}$ (3.68 Å) to $d_{(O-TM-O)}$ (2.75 Å) is 1.33, which is lower than in previously reported HEO424 (1.46, with a $d_{(O-Na-O)}$ of 3.18 Å and a $d_{(O-TM-O)}$ of 2.18 Å).[44] This lower ratio implies an increase in the stability of the layered structure, which is expected to delay the O3–P3 phase transition during desodiation. The diversity of the TMs, with their varied ionic sizes, results in the enlargement of the O—TM—O slabs, which further weakens the electrostatic repulsion between the TMO_2 layers and hence expands the channels for Na^+ transport.[44]

Sharp diffraction peaks along with bright selected-area electron diffraction (SAED) patterns (Figure 1b–d) indicative of high crystallinity for all three compositions, which suggests the occurrence of fewer side reactions, such as the intercalation of foreign ions and solvents.[31,45] Energy-dispersive X-ray spectroscopy mapping (Figures S7–S9, Supporting Information) shows that the distribution of elements (except Li) is homogeneous; however, the difference in intensity of elemental colors is due to different concentrations of elements. Furthermore from the survey XPS scan, it can be seen that all the elements including Li (Figure S10, Supporting Information) are successfully incorporated into the structure.

Scanning electron microscopy (SEM) images (Figure 1e–g) clearly reveal the layered structure of the compositions. High-resolution transmission electron microscopy (HRTEM) analysis of one of the compositions, $Na_{0.9}Li_{0.1}$HEO-F (Figure 1h; Figure S11, Supporting Information), reveals lattice fringes corresponding to interplanar distances of 5.5 and 2.8 Å associated with the (003) and (006) planes,[46] (Figure 1i; Figure S11, Supporting Information) which, along with the inverse Fast Fourier Transform (FFT) profile (Figure 1j; Figure S11, Supporting Information), are consistent with an O3-layered structure.

2.2. Electrochemical Performance (2–4 V)

The electrochemical performance of the three cathodes (Na_1Li_0, $Na_{0.9}Li_{0.1}$, and $Na_{0.8}Li_{0.2}$) was evaluated in the half-cell configuration in the range of 2–4 V. The initial charge/discharge profile at a current rate of 0.06 C is shown in **Figure 2**a. The first-charge specific capacity is 118, 105, 92, for Na_1Li_0, $Na_{0.9}Li_{0.1}$, and $Na_{0.8}Li_{0.2}$, which is equivalent to extracting 0.53, 0.42, and 0.32 Na^+ ions, respectively. The discharge capacity of Na_1Li_0 is lower than its charge capacity but for $Na_{0.9}Li_{0.1}$ and $Na_{0.8}Li_{0.2}$, the discharge capacity is higher than the charge capacity, which could be due to the presence of Na^+ vacancies that can accommodate more Na^+ ions.[3] The discharge curves of all three compositions were compared and analyzed to estimate the fraction of O- and P-type phases, as shown in Figure S12 (Supporting Information).

© 2023 The Authors. Advanced Materials published by Wiley-VCH GmbH

The slope in the discharge curve is recognized as being characteristic of the P-type phase and the plateau of the O-type phase.[27] From the discharge curve, $Na_{0.9}Li_{0.1}$ exhibits the highest contribution from the O-type phase, which explains why $Na_{0.9}Li_{0.1}$ has the highest discharge capacity. Other than this, there is a slope at the lower potential (1.95 V) of the discharge curve of $Na_{0.9}Li_{0.1}$ and $Na_{0.8}Li_{0.2}$ which is associated with the Mn^{4+}/Mn^{3+} redox reaction.[47,48] This disproportionation of Mn at the discharged state is prominent for $Na_{0.8}Li_{0.2}$ as can observed from the discharge curve. To further validate this, Mn2p spectra of $Na_{0.9}Li_{0.1}$ and $Na_{0.8}Li_{0.2}$ (Figure S13, Supporting Information) are analyzed after 3 initial cycles at C/15 rate, from which Mn^{3+}/Mn^{4+} is found to be larger in case of $Na_{0.8}Li_{0.2}$ which could be detrimental for the structure during long-term cycling.

Furthermore, Na_1Li_0, $Na_{0.9}Li_{0.1,}$ and $Na_{0.8}Li_{0.2}$ demonstrate reversible capacities at all rates, as evident from the charge/discharge profiles (Figures S14–S16, Supporting Information). The rate performance was then evaluated by comparing the discharge capacities exhibited by the three compositions at current rates ranging from 0.06 C to 3 C. As shown in Figure 2b, $Na_{0.9}Li_{0.1}$ and Na_1Li_0 have almost identical discharge capacities at all rates, whereas the capacity of $Na_{0.8}Li_{0.2}$ is consistently ≈10–15% lower. The low Na content of $Na_{0.8}Li_{0.2}$ is the cause for its low capacity. The rate capabilities obtained from 0.06 C to 3 C are almost similar (≈72%) for all compositions. In addition, it is observed that during the rate performance test, the capacity retention at 0.1 C is a little higher than the initial capacity which could be attributed to the activation process such as more wetting of the cathode by the electrolyte when the cathode is subjected to the different current rate.[49] Not only does $Na_{0.9}Li_{0.1}$ show the best retention of capacity at 0.1 C (measured before and after the rate performance test), but it also manifests stable cycling at 0.2 C: it has a 98% capacity retention (after undergoing all the rate changes), compared to 93% and 92% for $Na_{0.8}Li_{0.2}$ and Na_1Li_0, respectively.

The studies indicate a substantially improved structural stability of the high-entropy $Na_{0.9}Li_{0.1}$ structure. To confirm that cycle life was improved, $Na_{0.9}Li_{0.1}$ was examined over 200 cycles. Figure 2c provides a comparative cycling behavior at 0.5 C after initial activation of 5 cycles at 0.06 C. $Na_{0.9}Li_{0.1}$ and $Na_{0.8}Li_{0.2}$ exhibit capacity retention of 90%, compared to 81% for Na_1Li_0 (Figures S17–S19, Supporting Information). ICP-OES studies (Table S5, Supporting Information) are carried out on the anode (sodium) which points toward the leaching of Fe for Na_1Li_0, however, Li substituted $Na_{0.9}Li_{0.1}$ and $Na_{0.8}Li_{0.2}$ does not show trace of redox-active metals. Even after 300 cycles, $Na_{0.9}Li_{0.1,}$ still retains a capacity of 80% (Figure S20, Supporting Information), as can be seen from the charge–discharge profile. This high capacity retention is attributed to the high entropy effect which induces the homogeneous distribution of transition metals at a single site, resulting in more active sites, less strain accumulation, and therefore better interparticle stability.[46] The comparatively low cycling stability of Na_1Li_0, despite its high initial discharge capacity, is due to the structural destabilization after Na extraction. By contrast, in the other two compositions, Li inclusion and the associated Na vacancies improve the structural integrity of the material and facilitate the diffusion of Na^+ ions; this was confirmed by the results from the galvanostatic intermittent titration technique (GITT) analysis (Figure 2f).

Further to this, the effect of adding Li to the structure on the CEI formation was investigated by comparing the post-cycling C1s XPS spectra of the three compositions at 2–4 V (Figure S21, Supporting Information). The observed C1s spectrum is deconvoluted into five peaks positioned at 284.8 eV, corresponding to C—C/C═C of conductive carbon; 286.35 eV, for C—H; 291.35, for C—F of the PVDF binder; 287.56 for C—O; and 289.3 for carbonate species on the cathode surface. Careful comparative analysis of the XPS spectra reveals that with the introduction of Li, the area under the curve belonging to C—O and carbonate species decreases. The lower area of C—O and carbonate peaks point toward the suppression of both interfacial parasitic reactions and electrolyte degradation at the cathode surface with Li inclusion in the structure, ultimately resulting in the lower carbonate content in the CEI.[50]

Though Lithium substituted composition shows better cyclic stability, the mechanical stress due to repeated desodiation–sodiation may generate cracks enabling the penetration of electrolyte and could result in deterioration of the structure. Therefore, post-mortem analysis (Figure S22a, Supporting Information) after 50 cycles (2–4 V) of charge–discharge for all three compositions is carried out. Cross-sectional image reveals a more prominent presence of the low density of cracks in Na_1Li_0 and $Na_{0.8}Li_{0.2}$ that can accelerate capacity decay. However SAED pattern (Figure S22b, Supporting Information) reveals the retention of structure. For more clarity on structural deterioration, Impedance after initial low rate cycles as well as after 50 cycles (@C/2) is studied (Figure S22c,d, Supporting Information). After initial low rate cycles, the Nyquist plot shows a higher R_{CT} of $Na_{0.9}Li_{0.1}$ as compared to the other two which could be due to the formation of the CEI layer. Further after the high rate 50 cycles, all three cathodes exhibited a double semicircle feature attributed to the charge transfer process at the two interfaces electrolyte/CEI and CEI/cathode.[51] $Na_{0.9}Li_{0.1}$ shows the lowest charge transfer resistances that explain the highest capacity retention ability. The difference in charge transfer resistances of Li-substituted cathodes might be due to the more prominent disproportionation redox reaction of Mn^{4+} in $Na_{0.8}Li_{0.2}$ that accelerates the structural distortion.

The mean voltages at the beginning of the cycling at a 0.5 C rate and after 150 cycles were determined (Figure 2d). Initially, $Na_{0.8}Li_{0.2}$ exhibits the lowest mean voltage, whereas after cycling, $Na_{0.9}Li_{0.1}$ shows the lowest voltage increment voltage hysteresis (Figure 2e), indicating a lower polarization, high Na^+ ion reversibility, and a more stable crystal structure and is in agreement with the impedance outcomes.[52] The above results prove the combined usefulness of high entropy and Li substitution in the design of the cathode.

To further evaluate the contribution of Li in enhancing the diffusive properties, Na^+ diffusion coefficients were determined from GITT curves (Figures S23–S25, Supporting Information) recorded at a 0.06 C rate and then plotted against voltage (Figure 2f). The inclusion of lithium into the crystal structure enhances the diffusivity of Na^+ ions, supporting the theory that incorporation of Li^+ into the structure increases the number of Na^+ vacancies, leading to higher diffusion. At 4 V, the diffusion coefficients of $Na_{0.9}Li_{0.1}$ and $Na_{0.8}Li_{0.2}$ are very similar, in the range $(3–4) \times 10^{-10}$, and higher than that of Na_1Li_0. Although

© 2023 The Authors. Advanced Materials published by Wiley-VCH GmbH

15214095, 2023, 51, Downloaded from https://onlinelibrary.wiley.com/doi/10.1002/adma.202304440 by Indian Institute Of Technology , Wiley Online Library on [16/04/2024]. See the Terms and Conditions (https://onlinelibrary.wiley.com/terms-and-conditions) on Wiley Online Library for rules of use; OA articles are governed by the applicable Creative Commons License

15214095, 2023, 51, Downloaded from https://onlinelibrary.wiley.com/doi/10.1002/adma.202304440 by Indian Institute Of Technology, Wiley Online Library on [16/04/2024]. See the Terms and Conditions (https://onlinelibrary.wiley.com/terms-and-conditions) on Wiley Online Library for rules of use; OA articles are governed by the applicable Creative Commons License

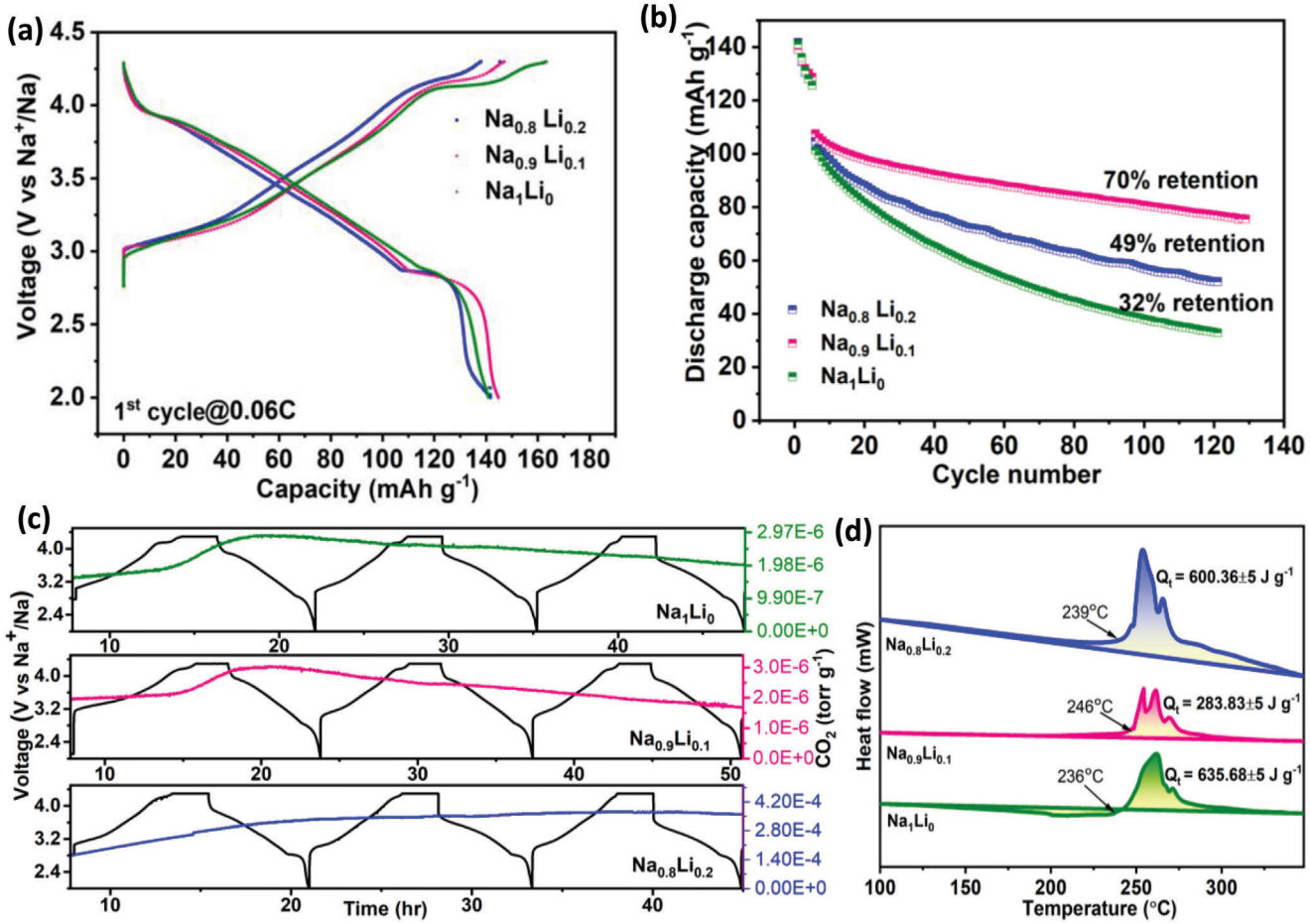

Figure 3. Comparative electrochemical performance in half-cells in the range 2–4.3 V vs Na/Na^+. a) First formation cycle. b) Cycle life studies at discharge rate 0.5 C (initial at 0.06 C). c) CO_2 gas evolution studies during the first three cycles at 0.06 C. d) Heat flow vs temperature plots measured by DSC method with electrolyte solution (1 M $NaClO_4$ in EC: PC::4:6 v/v% + 2%FEC).

$Na_{0.8}Li_{0.2}$ shows good diffusibility during the initial cycles, charge storage is comparatively low in $Na_{0.8}Li_{0.2}$ due to the less sodium in the structure and with continued cycle test, disproportionation of Mn^{4+} deteriorates the structure which is evident from the determined increasing polarization. Overall, the electrochemical performance of $Na_{0.9}Li_{0.1}$ surpasses the performance of the other compositions.

We established that the Na/Li ratio in $Na_{0.9}Li_{0.1}$ results in the best performances; however, the composition of redox-active elements strongly influences the performances as well. Therefore, to evaluate whether other variations in the designed composition could improve the performance of this structure, other compositions with different concentrations of Ni, Fe, and Mn were synthesized in similar conditions (Supporting Information). It is concluded that Ni and Fe clearly contribute predominantly to capacity than Mn (Figures S26–S31, Supporting Information). These outcomes show the impact of the cocktail effect of the high-entropy approach on the electrochemical properties and how this effect can be exploited by optimizing the composition of the HE material. Also in the compositions where Mn is increased, $Mn^{4+}/^{3+}$ redox behavior is found to be enhanced indicated by the slope in the discharge curve at lower potential. This also validates that $Na_{0.9}Li_{0.1}Ni^{2+}_{0.4}Fe^{3+}_{0.2}Mn^{2+}_{0.4}Ti^{4+}_{0.04}Mn^{4+}_{0.04}Mg^{2+}_{0.02}O_{1.9}F_{0.1}$ is the best-optimized composition.

2.3. Electrochemical Performance (2–4.3 V)

It is well documented that a higher charge cut-off voltage triggers an oxygen redox reaction with irreversible oxygen loss, causing structural decay.[53] Furthermore, at high voltages, the evolved oxygen results in the formation of reactive oxygen species, which catalyzes electrolyte degradation and other parasitic reactions severely impeding the stability and performance of the material. Therefore, the stability of the proposed high-entropy structures was further investigated by studying the electrochemical behavior under more aggressive conditions by increasing the charging cut-off voltage from 4.0 to 4.3 V. As shown in **Figure 3**a, $Na_{0.9}Li_{0.1}$ and $Na_{0.8}Li_{0.2}$ display similar initial charge–discharge capacities of 144 and 141 mAh g^{-1} respectively. Unlike Na_1Li_0, both Li-containing HEO-F materials exhibit a plateau ≈3 V corresponding to an O3–P3 phase transition during charging. Another plateau ≈2.7 V was observed during discharging, which implies the recovery of the initial O3

© 2023 The Authors. Advanced Materials published by Wiley-VCH GmbH

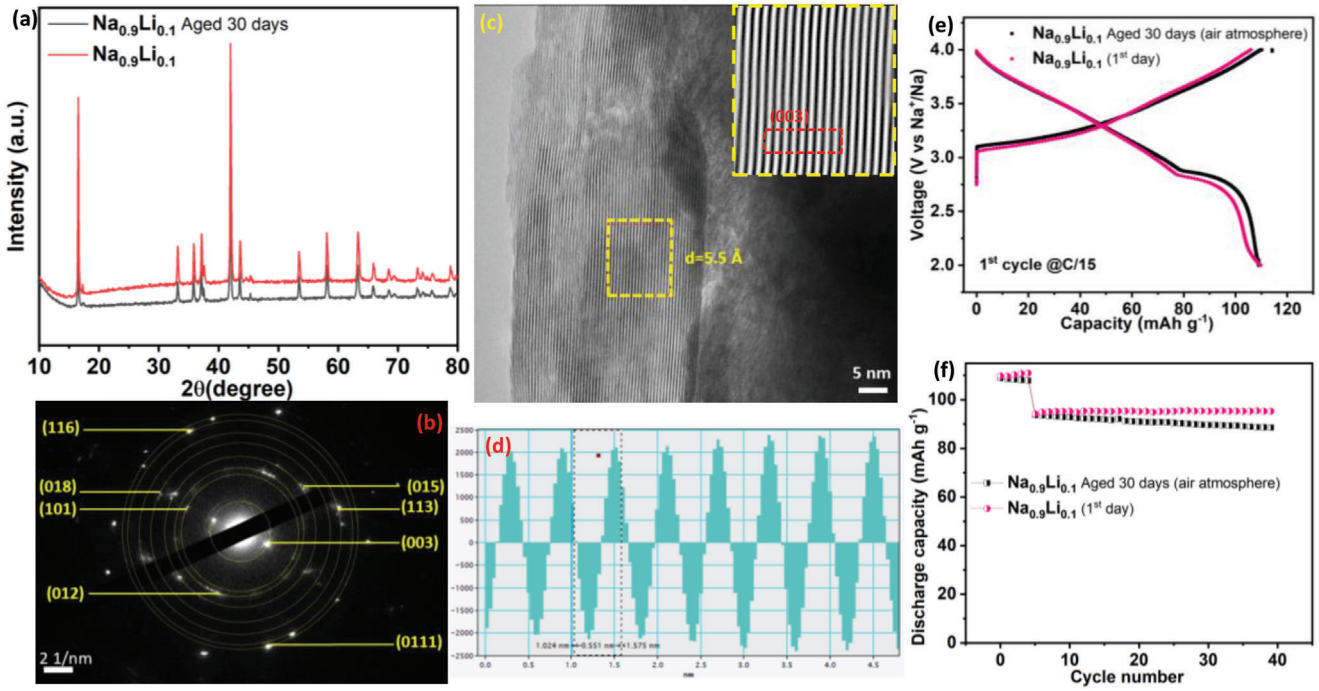

Figure 4. a) XRD pattern of initial and aged $Na_{0.9}Li_{0.1}$. b) SAED pattern of aged $Na_{0.9}Li_{0.1}$. c) HRTEM image of aged $Na_{0.9}Li_{0.1}$ (inset: inverse FFT of the selected region). d) Line profile of the selected IFFT region. e) Comparison between the first cycle of aged $Na_{0.9}Li_{0.1}$ and that of the initial $Na_{0.9}Li_{0.1}$ (2–4 V). f) Comparison of capacity retention during cycling at 0.5 C discharge rate (initial at 0.06 C).

phase, showing the excellent reversibility of the phase transition. This can be explained by the formation of a superstructure leading to Li–TM interactions stabilizing the O lattice in the structure.[38,53] The long-term cycling results shown in Figure 3b clearly demonstrate that the cathode without Li suffers from severe capacity fading, whereas $Na_{0.9}Li_{0.1}$ shows much higher capacity retention; 70%. Of note, such a high cut-off voltage requires further modification of the cathode surface or electrolyte in order to become relevant for practical applications, yet our finding clearly emphasizes the effect of composition on material's stability; the 70% capacity retention exhibited by $Na_{0.9}Li_{0.1}$—more than twice as high as that of Na_1Li_0—confirms the substantial improvement in the stability of the HEO-F material.

A voltammetric study of the three compositions was conducted over two cycles at a similar rate (Figure S32, Supporting Information). Three pairs of clear reversible redox peaks are observed for $Na_{0.9}Li_{0.1}$ and $Na_{0.8}Li_{0.2}$, corresponding to a three-step transition of Na^+ extraction/insertion owing to the redox reaction of Ni, Fe, and Mn. We propose that the stability enhancement in the presence of Li is due to the stabilization of the O lattice, Li–TM interactions, and the increased ionic character of the TM—F bond in Li-containing HEO-F materials. Additionally, because of the stabilization of the O lattice, electrolyte degradation at the electrode/electrolyte interface at such high potentials is expected to be much lower than in Li-free HEO-Fs.

The O-assisted degradation of carbonate-based electrolytes results in the release of CO_2 as a byproduct.[54] Therefore, to compare the extent of electrolyte degradation, the evolution of carbon dioxide in response to the applied potential was monitored using operando online electrochemical mass spectroscopy. All three compositions show no trace of evolved oxygen, a major cause of electrolyte decomposition (Figures S33–S35, Supporting Information), illustrating the role of the high-entropy stabilization of the crystal structure at the high voltage of 4.3 V. On the other hand, the evolution of CO_2 gas is detected from Na_1Li_0, $Na_{0.9}Li_{0.1}$, and $Na_{0.8}Li_{0.2}$ at the first cycle ≈3.4 V (Figure 3c). Hence, it can be concluded that CO_2 is not produced by the decomposition of the electrolyte but from the carbonate species on the surface of the cathode from air contamination.[29,55] The inclusion of Li^+ ions introduces Na^+ vacancies in the composition, which further results in a reduced interaction of the cathode with the air. Therefore, a smaller amount of CO_2 is evolved for $Na_{0.8}Li_{0.2}$. The thermal behavior which is a vital indicator of practical implication was studied by differential scanning calorimetric (DSC) measurements for all three compositions. In this measurement, heat evolution is recorded which is caused by thermochemical interaction between electrode and electrolyte on going to a steady temperature rise from room temperature to 350 °C. The exothermic heat evolution occurs due to the thermal decomposition of electrolytes and the thermochemical reactions involving lattice oxygen molecules of cathode and electrolytic species.[56] Figure 3d shows the results of Na_1Li_0, $Na_{0.9}Li_{0.1}$, and $Na_{0.8}Li_{0.2}$ cathodes charged to 4.3 V (desodiated) without elimination of electrolyte. The exothermic peak of Li-substituted cathodes is found to be at higher temperature with less release of heat. Among Li-substituted cathodes, $Na_{0.9}Li_{0.1}$ indicates a significantly lower heat release which shows that optimized Li substitution suppresses the side reaction between cathode and electrolyte and hence inhibits the structural degradation to avoid the thermal runaway.

© 2023 The Authors. Advanced Materials published by Wiley-VCH GmbH

15214095, 2023, 51, Downloaded from https://onlinelibrary.wiley.com/doi/10.1002/adma.202304440 by Indian Institute Of Technology, Wiley Online Library on [16/04/2024]. See the Terms and Conditions (https://onlinelibrary.wiley.com/terms-and-conditions) on Wiley Online Library for rules of use; OA articles are governed by the applicable Creative Commons License

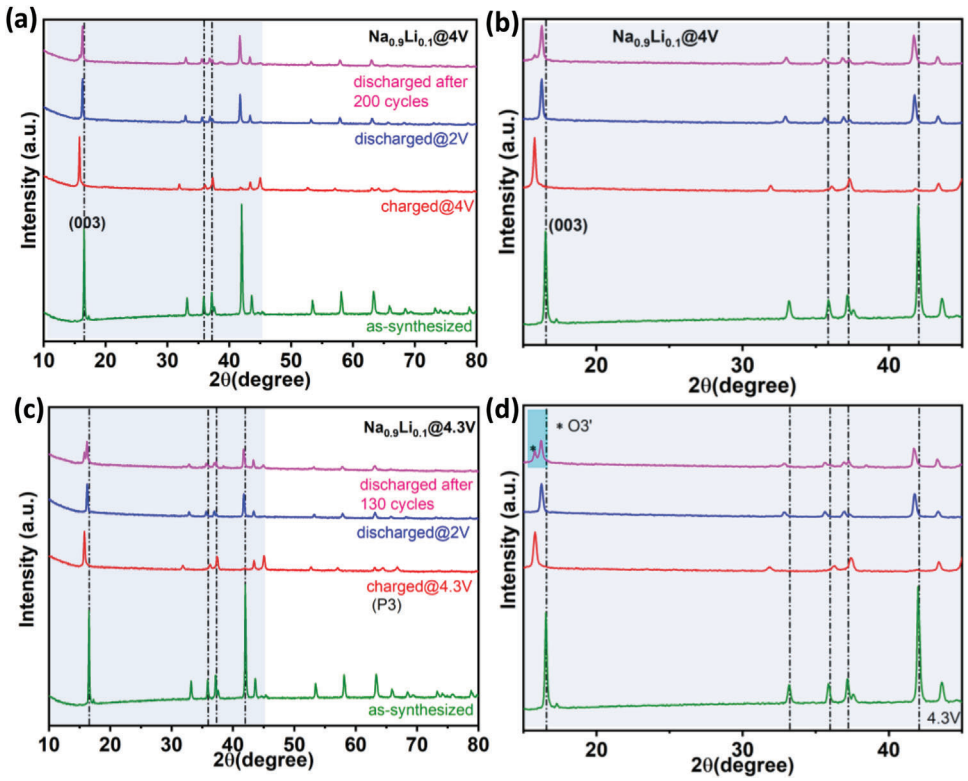

Figure 5. a–d) Ex situ XRD pattern of $Na_{0.9}Li_{0.1}$ in the charged state, discharged state, and after prolonged cycling. a) Overall spectrum and b) region of interest at 2–4 V (after 200 cycles); c) overall spectrum and d) region of interest at 2–4.3 V (after 130 cycles).

The influence of fluorine was also evaluated; a composition without fluorine and having the same O3-layered structure was synthesized and named (—F) $Na_{0.9}Li_{0.1}$ (Figure S36, Supporting Information). Though its initial discharge capacity is slightly higher (Figure S37a, Supporting Information), the fluorine-free material experiences a steep decline in capacity during long-term cycling (Figure S37b, Supporting Information). Moreover, ex situ diffraction pattern is recorded at charged, discharged state as well as after long-term cycling (Figure S38, Supporting Information). It is observed that on initial charge and discharge state, there is a reversible phase transition between O- and P-type phase, although on prolonged cycling O3 phase is not completely recovered. Further on thermal behavior analysis by DSC (Figure S39, Supporting Information), it is found that without fluorine thermal activity is at a much higher early onset temperature and almost double of heat release than cathode substituted with fluorine. This shows that fluorine substitution improves the structural stability of the cathode on interaction with electrolyte and also increases the thermal abuse tolerance.

2.4. Air Stability of the $Na_{0.9}Li_{0.1}$ Cathode

Because of their high Na content, O3-layered materials are largely considered the most promising cathodes for practical sodium-ion batteries. Still, two important factors act as roadblocks to the commercialization of these materials, namely, sluggish kinetics and air sensitivity. When the O3 material is exposed to air, Na^+ ions from the lattice escape to the surface and react with water and CO_2 to form residual alkali species, which further affects the kinetic performance and reduces the capacity of the cell.[12]

Here, with the introduction of Li in the material, the interlayer distance increases, as already mentioned (the "c" parameter increases), because of a decrease in the shielding effect of the positively charged Na ions, which in turn improves the kinetic performance, as depicted by the GITT results. Along with this, in the above-mentioned studies, we found that the valence state of the transition metals also increases (the "a" parameter decreases) and so does the oxidation resistance of the material, thus suppressing unwanted reaction with air.[36] XPS studies show that for the C1s spectra (Figure S40, Supporting Information), the peak corresponding to carbonate species is significantly reduced in $Na_{0.9}Li_{0.1}$ and $Na_{0.8}Li_{0.2}$ as compared to Na_1Li_0.

An XRD trace of the $Na_{0.9}Li_{0.1}$ cathode recorded after 30 days of air exposure confirms the stability of the crystal structure; no impurity was detected (**Figure 4**a). The SAED bright pattern, indexed to planes of the initial O3-layered structure (Figure 4b), further validates the stability of the structure after aging in the air. HRTEM of the aged cathode clearly shows the lattice fringes of the (003) plane (Figure 4c,d), as for the pre-aging $Na_{0.9}Li_{0.1}$. In addition, the initial charge/discharge (Figure 4e) electrochemical behavior of $Na_{0.9}Li_{0.1}$ after aging exactly matches that before aging. Hence, the designed cathode, thanks to the above modifications (high valence state of TMs), exhibits excellent air

© 2023 The Authors. Advanced Materials published by Wiley-VCH GmbH

15214095, 2023, 51, Downloaded from https://onlinelibrary.wiley.com/doi/10.1002/adma.202304440 by Indian Institute Of Technology, Wiley Online Library on [16/04/2024]. See the Terms and Conditions (https://onlinelibrary.wiley.com/terms-and-conditions) on Wiley Online Library for rules of use; OA articles are governed by the applicable Creative Commons License

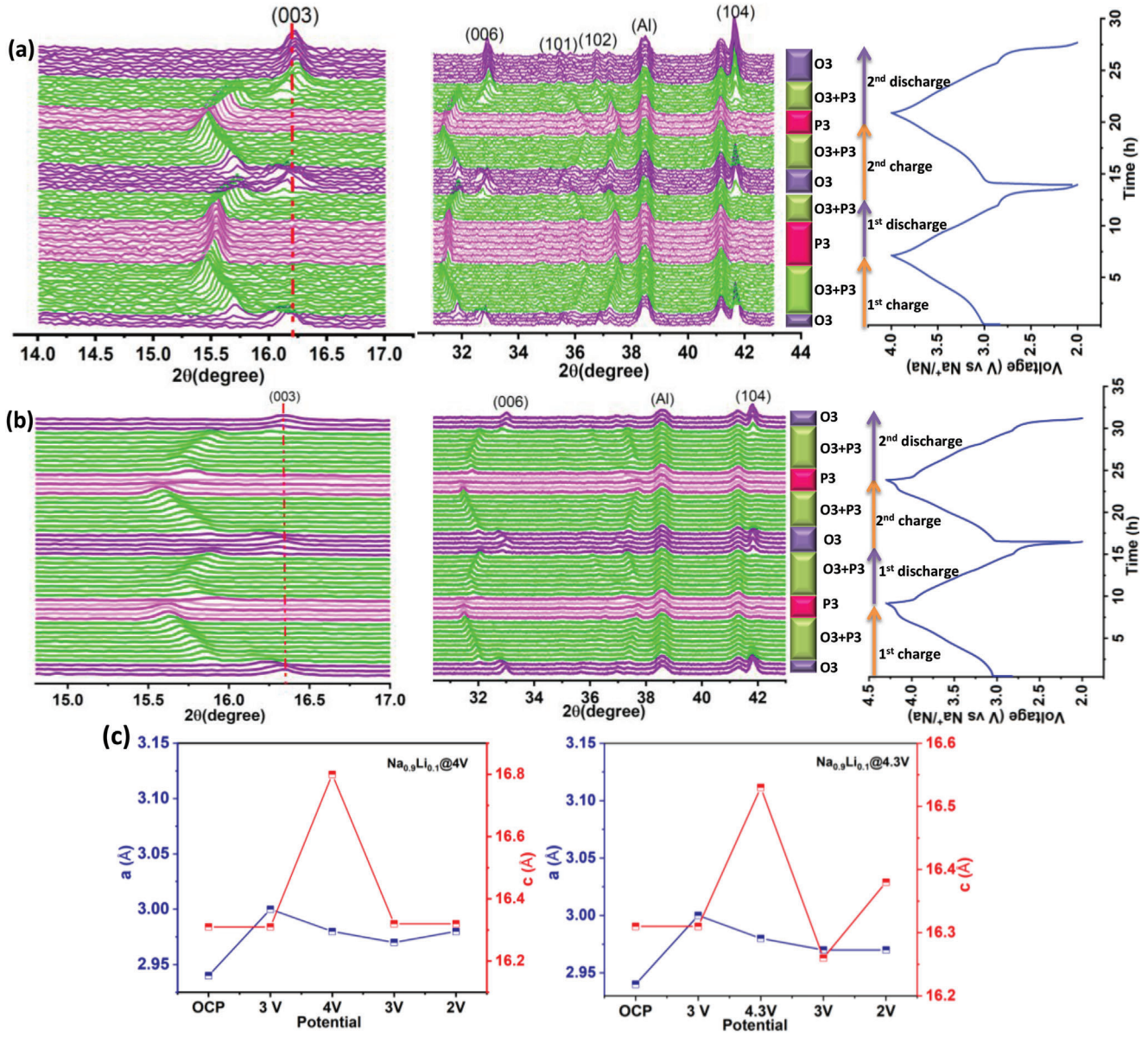

Figure 6. a,b) In situ XRD pattern of $Na_{0.9}Li_{0.1}$ during the two initial charge/discharge cycles and corresponding voltage profiles in the ranges 2–4 V (a) and 2–4.3 V (b). c) Calculated lattice parameters at different charged/discharged states.

stability, which could be a significant factor in reducing the overall cost of cathode storage. Although cycle studies (Figure 4f) show a slight decrease in performance at the high rate of 0.5 C, the performance of $Na_{0.9}Li_{0.1}$ remains satisfactory.

The above results demonstrate that not only does the introduction of Li stabilize the crystal structure during sodiation/desodiation, but it also improves the kinetic and air sensitivity of the designed cathode.

2.5. Structural Evolution during the Electrochemical Reaction

Understanding the structural evolution of the HEO-F cathode during charge/discharge is a prerequisite for recognizing the mechanism governing the desodiation/sodiation process. Therefore, ex situ XRD measurements at the two voltage ranges discussed earlier (2–4 and 2–4.3 V) were conducted at the first charge–discharge cycle (0.06 C) and after long-term cycling at a 0.5 C discharge rate. Generally, in O3-type oxides; a transition between the O- and P-type phases occurs during the desodiation/sodiation process because of the slab gliding in the direction perpendicular to the c axis. From the ex situ XRD, on charging to either 4 V (**Figure 5**a,b) or 4.3 V (Figure 5c,d), the (003) peak clearly shifts to lower angles, implying an expansion of the *c*-axis, and the appearance of a P3 phase. Along with this, the (104) peak diminishes on charging, again confirming the transition from the O3 phase to the P3 phase. Furthermore, the (104) peak reappears on discharging, indicating that the structure returns

© 2023 The Authors. Advanced Materials published by Wiley-VCH GmbH

15214095, 2023, 51, Downloaded from https://onlinelibrary.wiley.com/doi/10.1002/adma.202304440 by Indian Institute Of Technology, Wiley Online Library on [16/04/2024]. See the Terms and Conditions (https://onlinelibrary.wiley.com/terms-and-conditions) on Wiley Online Library for rules of use; OA articles are governed by the applicable Creative Commons License

15214095, 2023, 51, Downloaded from https://onlinelibrary.wiley.com/doi/10.1002/adma.202304440 by Indian Institute Of Technology , Wiley Online Library on [16/04/2024]. See the Terms and Conditions (https://onlinelibrary.wiley.com/terms-and-conditions) on Wiley Online Library for rules of use; OA articles are governed by the applicable Creative Commons License

to an O3-type layered structure, although the (003) and (104) peaks do not return to their exact initial positions; the fully discharged phase is an O3-type phase but with a larger interlayer distance in the NaO_2 slabs compared to the phase in as-synthesized $Na_{0.9}Li_{0.1}$. Besides, owing to disturbed long-range order during the transition, the diffraction peaks appear weaker. Overall, the phase transition from O3 to P3 is largely reversible at both voltage ranges.

To further evaluate the stability of the cathode structure during the electrochemical process, an XRD pattern was recorded after long-term cycling. No change is seen after cycling for the Na_1Li_0 electrode at 2–4 V (after 200 cycles) and 2–4.3 V (after 130 cycles), except for the splitting of the (003) peak, which is a characteristic of an (O3 + O3′)-type phase. The O3- and O3′-type phases share the same rhombohedral structure, which could explain the performance degradation during cycling.[57] The XRD patterns show a much lower proportion of the O3′ phase in $Na_{0.9}Li_{0.1}$ than in Na_1Li_0 in the 4 V charged state, which indicates that with the addition of Li, the complex phase transition is largely suppressed (Figure S41, Supporting Information). For $Na_{0.8}Li_{0.2}$ (Figure S42, Supporting Information), the transition from the charged to the discharged state is similar to that in $Na_{0.9}Li_{0.1}$, with even less O3′ phase present in the 4 V charged state.

To obtain further confirmation of the structural evolution during the charge and discharge of $Na_{0.9}Li_{0.1}$, in situ, XRD was conducted at the two previously mentioned voltage ranges for two charge/discharge cycles at a 0.06 C rate (**Figure 6**a,b). At the beginning of charging, as sodium is deintercalated, the (003) and (006) peaks shift to lower angles and the (104) peak intensity decreases, indicating the transition from an O-type phase to a P-type phase. Usually, the transition from O3 to P3 occurs via an O3′ phase (O3–O3′–P3), but here, there is no indication of the O3′ monoclinic phase, which would be detected by the splitting of the (003) and (006) peaks.[58] Clearly, increasing the entropy of the cathode to a high-entropy level allows the suppression of the phase transition and thus improves the cathode's cyclic stability.

On complete charging, at 4 and 4.3 V, a complete P3 phase is seen, the (104) peak is absent, and the (003) peak is shifted to lower angles. The appearance of a P3 phase is associated with sodium vacancies and thus strong oxygen–oxygen (O–O) repulsions; the latter trigger a displacement of the TMO6 layers, which results in the creation of prismatic sodium positions.[59] Moreover, on discharging, the P3 phase returns to the original O3 phase, as shown by the return of the (003), (006), and (104) peaks to their initial positions; the phase transition is completely reversible.

With the phase transformation (O- to P-type), there is a change in the lattice parameters to sustain the structure. Desodiation results in the (003) and (006) peaks shifting to lower angles and the (101) and (102) peaks shifting to higher angles. This shifting of peaks is an indication of an increase in the "*c*" lattice parameter and a decrease in the "*a*" parameter (Figure 6c). The change in lattice parameters occurs because during charging, as transition metals are oxidized, their ionic size is reduced, resulting in a contraction of the "*ab*" plane. In parallel, an increase in electrostatic repulsion between adjacent oxygen layers results in the expansion of the "*c*" plane. Volume expansion also occurs on charging (123 to 129 $Å^3$ at 4 V and 127 $Å^3$ at 4.3 V); the volume returns to 125 $Å^3$ on discharging, with a change of only 1.6% after a charge–discharge cycle.

3. Conclusion

In the present work, all the shortcomings of the O3-layered structure, that is, complex phase transition, sluggish kinetics, poor air stability, and inferior capacity, were tackled using the introduction of the high-entropy approach. Most importantly, a Co-free O3-layered cathode for sodium-ion battery applications was synthesized using Ni, Fe, and Mn as redox-active participants. To achieve high entropy in the structure, Li was incorporated to introduce Na vacancies into the structure, which endowed the cathode with improved kinetics and a high capacity (109 mAh g^{-1} in the range 2–4 V; 139 mAh g^{-1} in the range 2–4.3 V). The formation of vacancies enlarges the interlayer distance and allows the facile diffusion of ions during sodiation/desodiation, thus maintaining the structural integrity of the cathode and suppressing the formation of an O3′ phase during the O3–P3 phase transition. The advantage of an enlarged Na-layer spacing is reflected in the high-rate capability of 72% (0.06 to 3 C) and stable capacity retention of 90% after 200 cycles. The formed vacancies also enhance the antioxidative ability of the cathode by decreasing the charge density of the transition metals. The impressive outcomes of this strategy show that it could open new avenues for reaching the performance requirements of practical applications.

Supporting Information

Supporting Information is available from the Wiley Online Library or from the author.

Conflict of Interest

The authors declare no conflict of interest.

Data Availability Statement

The data that support the findings of this study are available from the corresponding author upon reasonable request.

Keywords

air stability, cobalt-free cathodes, cocktail effect, high configuration entropy, sodium-ion batteries, O3-layered structure

Received: May 11, 2023
Revised: August 2, 2023
Published online: November 12, 2023

[1] J. W. Choi, D. Aurbach, *Nat. Rev. Mater.* **2016**, *1*, 16013.
[2] I. Hasa, D. Buchholz, S. Passerini, J. Hassoun, *ACS Appl. Mater. Interfaces* **2015**, *7*, 5206.
[3] Y. Wang, J. Liu, B. Lee, R. Qiao, Z. Yang, S. Xu, X. Yu, L. Gu, Y.-S. Hu, W. Yang, K. Kang, H. Li, X.-Q. Yang, L. Chen, X. Huang, *Nat. Commun.* **2015**, *6*, 6401.

© 2023 The Authors. Advanced Materials published by Wiley-VCH GmbH

[4] K. M. Abraham, *ACS Energy Lett.* **2020**, *5*, 3544.
[5] J. Molenda, A. Plewa, A. Kulka, Ł. Kondracki, K. Walczak, A. Milewska, M. Rybski, L. Lu, J. Tobola, *J. Power Sources* **2020**, *449*, 227471.
[6] E. Boivin, R. A. House, M. A. Pérez-Osorio, J. J. Marie, U. Maitra, G. J. Rees, P. G. Bruce, *Joule* **2021**, *5*, 1267.
[7] N. A. Katcho, J. Carrasco, D. Saurel, E. Gonzalo, M. Han, F. Aguesse, T. Rojo, *Adv. Energy Mater.* **2017**, *7*, 1601477.
[8] Y. Lu, L. Wang, J. Cheng, J. B. Goodenough, *Chem. Commun.* **2012**, *48*, 6544.
[9] B. Singh, Z. Wang, S. Park, G. S. Gautam, J. N. Chotard, L. Croguennec, D. Carlier, A. K. Cheetham, C. Masquelier, P. Canepa, *J. Mater. Chem. A* **2021**, *9*, 281.
[10] K. Walczak, A. Kulka, W. Zając, M. Ziąbka, R. Idczak, V. H. Tran, J. Molenda, *Appl. Mater. Interfaces* **2019**, *11*, 43046.
[11] P. F. Wang, Y. You, Y. X. Yin, Y. G. Guo, *Adv. Energy Mater.* **2018**, *8*, 1701912.
[12] R.-M. Gao, Z.-J. Zheng, P.-F. Wang, C.-Y. Wang, H. Ye, F.-F. Cao, *Energy Storage Mater.* **2020**, *30*, 9.
[13] M. Sathiya, Q. Jacquet, M. L. Doublet, O. M. Karakulina, J. Hadermann, J. M. Tarascon, *Adv. Energy Mater.* **2018**, *8*, 1702599.
[14] S. W. D. Gourley, T. Or, Z. Chen, *iScience* **2020**, *23*, 101505.
[15] Y. Ma, Y. Ma, S. L. Dreyer, Q. Wang, K. Wang, D. Goonetilleke, A. Omar, D. Mikhailova, H. Hahn, B. Breitung, T. Brezesinski, *Adv. Mater.* **2021**, *33*, 2101342.
[16] Y. Chen, H. Fu, Y. Huang, L. Huang, X. Zheng, Y. Dai, Y. Huang, W. Luo, *ACS Mater. Lett.* **2021**, *3*, 160.
[17] M. Qin, J. Gild, C. Hu, H. Wang, M. d. S. B. Hoque, J. L. Braun, T. J. Harrington, P. E. Hopkins, K. S. Vecchio, J. Luo, *J. Eur. Ceram. Soc.* **2020**, *40*, 5037.
[18] K. Gu, D. Wang, C. Xie, T. Wang, G. Huang, Y. Liu, Y. Zou, L. Tao, S. Wang, *Angew. Chem., Int. Ed.* **2021**, *60*, 20253.
[19] D. Wang, Z. Liu, S. Du, Y. Zhang, H. Li, Z. Xiao, W. Chen, R. Chen, Y. Wang, Y. Zou, S. Wang, *J. Mater. Chem. A* **2019**, *7*, 24211.
[20] P. Edalati, Q. Wang, H. R-Khosroshahi, M. Fuji, T. I. Kaveh Edalati, *J. Mater. Chem. A* **2020**, *8*, 3814.
[21] B. Zhao, Y. Du, Z. Yan, L. Rao, G. Chen, M. Yuan, L. Yang, J. Zhang, R. Che, *Adv. Funct. Mater.* **2023**, *33*, 2209924.
[22] J. W. Yeh, *JOM* **2013**, *65*, 1759.
[23] C. M. Rost, E. Sachet, T. Borman, A. Moballegh, E. C. Dickey, D. Hou, J. L. Jones, S. Curtarolo, J. P. Maria, *Nat. Commun.* **2015**, *6*, 8485.
[24] L. Lin, K. Wang, A. Sarkar, C. Njel, G. Karkera, Q. Wang, R. Azmi, M. Fichtner, H. Hahn, S. Schweidler, B. Breitung, *Adv. Energy Mater.* **2022**, *12*, 2103090.
[25] A. Sarkar, Q. Wang, A. Schiele, M. R. Chellali, S. S. Bhattacharya, D. Wang, T. Brezesinski, H. Hahn, L. Velasco, B. Breitung, *Adv. Mater.* **2019**, *31*, 1806236.
[26] Z. Lun, B. Ouyang, D.-H. Kwon, Y. Ha, E. E. Foley, T.-Y. Huang, Z. Cai, H. Kim, M. Balasubramanian, Y. Sun, J. Huang, Y. Tian, H. Kim, B. D. McCloskey, W. Yang, R. J. Clément, H. Ji, G. Ceder, *Nat. Mater.* **2021**, *20*, 214.
[27] C. Zhao, F. Ding, Y. Lu, L. Chen, Y. S. Hu, *Angew. Chem., Int. Ed.* **2020**, *59*, 264.
[28] D. Berardan, S. Franger, A. K. Meena, N. Dragoe, *J. Mater. Chem.* **2016**, *4*, 9536.
[29] E. de la Llave, E. Talaie, E. Levi, P. K. Nayak, M. Dixit, P. T. Rao, P. Hartmann, F. Chesneau, D. T. Major, M. Greenstein, D. Aurbach, L. F. Nazar, *Chem. Mater.* **2016**, *28*, 9064.
[30] J. Xu, D. H. Lee, R. l. J. Clément, X. Yu, M. Leskes, A. J. Pell, G. Pintacuda, X.-Q. Yang, C. P. Grey, Y. S. Meng, *Chem. Mater.* **2014**, *26*, 1260.
[31] Y. Cao, Q. Zhang, Y. Wei, Y. Guo, Z. Zhang, W. Huang, K. Yang, W. Chen, T. Zhai, H. Li, Y. Cui, *Adv. Funct. Mater.* **2020**, *30*, 1907023.
[32] Y. S. Moghadam, A. E. Kharbachi, Y. Hu, K. Wang, S. Belin, M. Fichtner, *ACS Mater. Lett.* **2023**, *5*, 125.
[33] V. Duffort, E. Talaie, R. Black, L. F. Nazar, *Chem. Mater.* **2015**, *27*, 2515.
[34] D. Buchholz, L. G. Chagas, C. Vaalma, L. Wu, S. Passerini, *J. Mater. Chem. A* **2014**, *2*, 13415.
[35] R. J. Clement, J. Billaud, A. R. Armstrong, G. Singh, T. Rojo, P. G. Bruce, C. P. Grey, *Energy Environ. Sci.* **2016**, *9*, 3240.
[36] X.-G. Yuan, Y.-J. Guo, L. Gan, X.-A. Yang, W.-H. He, X.-S. Zhang, Y.-X. Yin, S. Xin, H.-R. Yao, Z. Huang, Y.-G. Guo, *Adv. Funct. Mater.* **2022**, *32*, 2111466.
[37] C. Zhao, Q. Wang, Z. Yao, J. Wang, B. Sánchez-Lengeling, F. Ding, X. Qi, Y. Lu, X. Bai, B. Li, *Science* **2020**, *370*, 708.
[38] L. Yao, P. Zou, C. Wang, J. Jiang, L. Ma, S. Tan, K. A. Beyer, F. Xu, E. Hu, H. L. Xin, *Adv. Energy Mater.* **2022**, *12*, 2201989.
[39] Q. Wang, Y. Liao, X. Jin, C. Cheng, S. Chu, C. Sheng, L. Zhang, B. Hu, S. Guo, H. Zhou, *Angew. Chem., Int. Ed.* **2022**, *61*, e202206625.
[40] Z. Wu, Y. Ni, S. Tan, E. Hu, L. He, J. Liu, M. Hou, P. Jiao, K. Zhang, F. Cheng, J. Chen, *J. Am. Chem. Soc.* **2023**, *145*, 9596.
[41] L. Ni, R. Guo, S. Fang, J. Chen, J. Gao, Y. Mei, S. Zhang, W. Deng, G. Zou, H. Hou, X. Ji, *eScience* **2022**, *2*, 116.
[42] S. Wang, T. Cui, L. Shao, S. Yang, L. Yu, J. Guan, X. Shi, J. Cai, Z. Sun, *J. Colloid Interface Sci.* **2022**, *627*, 922.
[43] L. Yu, L. Shao, S. Wang, J. Guan, X. Shi, J. Cai, N. Tarasenko, Z. Sun, *Mater. Today Phys.* **2022**, *22*, 100593.
[44] F. Ding, C. Zhao, D. Xiao, X. Rong, H. Wang, Y. Li, Y. Yang, Y. Lu, Y.-S. Hu, *J. Am. Chem. Soc.* **2022**,*144*, 8286.
[45] J. Leng, Z. Wang, J. Wang, H.-H. Wu, G. Yan, X. Li, H. Guo, Y. Liu, Q. Zhang, Z. Guo, *Chem. Soc. Rev.* **2019**, *48*, 3015.
[46] C.-C. Lin, H.-Y. Liu, J.-W. Kang, C.-C. Yang, C.-H. Li, H.-Y. T. Chen, S.-C. Huang, C.-S. Ni, Y.-C. Chuang, B.-H. Chen, C.-K. Chang, H.-Y. Chen, *Energy Storage Mater.* **2022**, *51*, 159.
[47] J. Wang, S. L. Dreyer, K. Wang, Z. Ding, T. Diemant, G. Karkera, Y. Ma, A. Sarkar, B. Zhou, M. V. Gorbunov, A. Omar, D. Mikhailova, V. Presser, M. Fichtner, H. Hahn, T. Brezesinski, B. Breitung, Q. Wang, *Mater. Futures* **2022**, *1*, 035104.
[48] H. Xu, C. Cheng, S. Chu, X. Zhang, J. Wu, L. Zhang, S. Guo, H. Zhou, *Adv. Funct. Mater.* **2020**, *30*, 2005164.
[49] X. Liang, H. Kim, H.-G. Jung, Y.-K. Sun, *Adv. Funct. Mater.* **2021**, *31*, 2008569.
[50] T. Sharabani, S. Taragin, I. Perelshtein, M. Noked, A. Mukherjee, *Small* **2021**, *17*, 2104416.
[51] H. Fu, M. Xia, R. Qia, X. Liang, M. Zhao, Z. Zhang, X. Lu, G. Cao, *J. Power Sources* **2018**, *399*, 42.
[52] A. Saha, O. Shalev, S. Maiti, L. L. Wang, S. H. Akhille, B. Schmerling, S. Targin, M. Tkachev, X. Fan, M. Noked, *Mater. Today Energy* **2023**, *31*, 101207.
[53] J. Liu, R. Qi, C. Zuo, C. Lin, W. Zhao, N. Yang, J. Li, J. Lu, X. Chen, J. Qiu, M. Chu, M. Zhang, C. Dong, Y. Xiao, H. Chen, F. Pan, *Nano Energy* **2021**, *88*, 106252.
[54] S. Maiti, H. Sclar, Rosy, J. G., M. Talianker, M. Tkachev, M. Tsubery, X. Wu, M. Noked, B. Markovsky, D. Aurbach, *Energy Storage Mater.* **2022**, *45*, 74.
[55] L. Zhang, C. Tsolakidou, S. Mariyappan, J.-M. Tarascon, S. Trabesinger, *Energy Storage Mater.* **2021**, *42*, 12.
[56] S. Maiti, H. Sclar, X. Wu, J. Grinblat, M. Talianker, A. Kondrakov, B. Markovsky, D. Aurbach, *Energy Storage Mater.* **2023**, *56*, 25.
[57] L. Mu, X. Feng, R. Kou, Y. Zhang, H. Guo, C. Tian, C.-J. Sun, X.-W. Du, D. Nordlund, H. L. Xin, F. Lin, *Adv. Energy Mater.* **2018**, *8*, 1801975.
[58] P.-F. Wang, Y. You, Y.-X. Yin, Y.-G. Guo, *J. Mater. Chem. A* **2016**, *4*, 17660.
[59] K. Walczaka, A. Plewa, C. Ghica, W. Zając, A. Trenczek-Zając, M. Zając, J. Toboła, J. Molenda, *Energy Storage Mater.* **2022**, *47*, 500.

© 2023 The Authors. Advanced Materials published by Wiley-VCH GmbH

15214095, 2023, 51, Downloaded from https://onlinelibrary.wiley.com/doi/10.1002/adma.202304440 by Indian Institute Of Technology , Wiley Online Library on [16/04/2024]. See the Terms and Conditions (https://onlinelibrary.wiley.com/terms-and-conditions) on Wiley Online Library for rules of use; OA articles are governed by the applicable Creative Commons License